Phase transition, equation of state, and limiting shear viscosities of hard sphere dispersions

See-Eng Phan and William B. Russel
Department of Chemical Engineering, Princeton University, Princeton, New Jersey 08544

Zhengdong Cheng, Jixiang Zhu, and Paul M. Chaikin
Department of Physics, Princeton University, Princeton, New Jersey 08544

John H. Dunsmuir
Exxon Research & Engineering Company, Annandale, New Jersey 08801

Ronald H. Ottewill
School of Chemistry, University of Bristol, Bristol, England

(Received 18 July 1996)

Despite an interparticle potential consisting of only an infinite repulsion at contact, the thermodynamics and dynamics of concentrated dispersions of hard spheres are not yet fully understood. Colloidal poly-(methyl methacrylate) spheres with a grafted layer of poly-(12-hydroxy stearic acid) (PMMA-PHSA) comprise a common model for investigating structural, dynamic, and rheological properties. These highly monodisperse spheres can be index matched in nonaqueous solvents, reducing van der Waals forces and allowing characterization via light scattering. In this work, we test the behavior of these dispersions against expectations for hard spheres through observations of the phase behavior, x-ray densitometry of equilibrium sediments, and Zimm viscometry. We set the effective hard sphere volume fraction by the disorder-order transition, thereby accounting for the polymer layer, any swelling due to the solvent, and polydispersity. The melting transition then occurs close to the expected value and the equation of state for the fluid phase, extracted from the equilibrium sediment with x-ray densitometry, conforms to the Carnahan-Starling equation. However, the osmotic pressure of the crystalline phase lies slightly above that calculated for a single fcc crystal even after accounting for polydispersity. Likewise the high shear viscosity of the fluid compares well with other hard sphere dispersions, but the low shear viscosity for PMMA-PHSA hard spheres exceeds those for polystyrene and silica hard spheres, e.g., a relative viscosity of 45 ± 3 at $\phi=0.50$ rather than 24. Our low shear viscosities are consistent with other PMMA-PHSA data after rescaling for both the polymer layer thickness and polydispersity, and may represent the true hard sphere curve. We anticipate that the equation of state for the crystal deviates due to polycrystallinity or a direct effect of polydispersity. [S1063-651X(96)11612-3]

PACS number(s): 82.70.Dd, 83.10.−y

I. INTRODUCTION

Concentrated colloidal dispersions, which form the backbone of many everyday materials such as paints, cosmetics, soil, plastics, and ceramics, exhibit a first order phase transition from a disordered fluid to an ordered crystal as well as a glass transition, and many other features analogous to atomic and molecular fluids. Consequently, understanding and manipulating their properties is of practical and academic interest [1–4].

Hard spheres, one of the most fundamental systems, feel no interparticle force except an infinite repulsion at contact, and provide a convenient model for understanding the structure and dynamics of many concentrated colloidal dispersions. One realization of this model system consists of a poly-(methyl methacrylate) (PMMA) sphere with a grafted layer of poly-(12-hydroxy stearic acid) (PHSA) chains dispersed in a good solvent for PHSA such as decalin and tetralin. The solvent is chosen so as to index match the particles and reduce the long-range van der Waals attraction. The branched PHSA chains provide a sufficiently thick layer to render the remaining van der Waals potential insignificant compared to the thermal energy. Thermodynamic and dynamic properties then depend on an effective volume fraction ϕ that accounts for the PHSA layer and, consequently, exceeds the volume fraction ϕ_c based on the PMMA core. Most recent studies with PMMA-PHSA dispersions convert from core to effective volume fraction by identifying the observed disorder-order transition with that predicted, i.e., setting $\phi=0.494$ at freezing [3,5]. This represents a thermodynamic definition of the effective volume fraction determined at the high concentrations of primary interest. Others [6] follow the earlier practice established with polystyrene and silica hard spheres of taking the inverse of the intrinsic viscosity $[\eta]$ as a measure of specific volume and setting $\phi=[\eta]\phi_c/2.5$, providing a hydrodynamic definition of the hard sphere in the dilute limit. The procedure of Pusey and van Megen has obvious advantages due to the difficulty of measuring $[\eta]$ accurately and the sensitivity of thermodynamic and transport properties to small shifts in ϕ at high concentrations.

To characterize the force between the PMMA-PHSA spheres, Cairns *et al.* [7] measured the excess osmotic pressure Π with spheres of diameter $2a=155$ nm in dodecane at

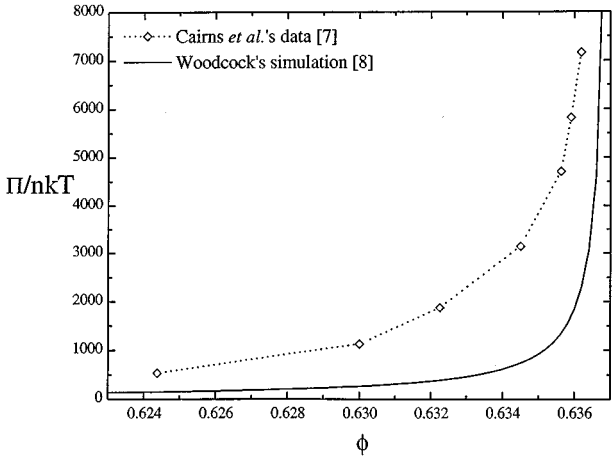

FIG. 1. Excess osmotic pressure measured with a compression cell vs ϕ for 155-nm-diameter PMMA-PHSA particles in dodecane [7] compared with Woodcock's simulation [8].

various ϕ_c with a custom built compression cell. For $\phi_c<0.53$, the osmotic pressure was barely detectable, and could not be quantified because of experimental difficulties at these very low pressures. The pressure then rises sharply for $\phi_c>0.53$ and essentially diverges at $\phi_c=0.566$, indicating close packing with a strong short-range repulsion (Fig. 1). The second curve on Fig. 1 corresponds to the osmotic pressure

$$\frac{\Pi}{nkT}=\frac{2.89}{1-\phi/\phi_{\max}}, \tag{1}$$

where kT is the thermal energy, n number density, and $\phi_{\max}=0.637$, which Woodcock [8] extracted from his simulations of metastable disordered hard spheres. Here we set $\phi=0.637/0.566\phi_c=1.125\phi_c$ to match the divergence in Cairns *et al.*'s data. This scaling implies an effective layer thickness of $L\sim3.3$ nm, much less than the 6–20 nm deduced from other measures of the effective hard sphere volume fraction. Indeed, comparison of the data and theoretical curve clearly suggests a longer-range softness in the potential, presumably due to compression or interpenetration of the grafted layers. Of course, increasing the radius of the particle core reduces the effect of the compressibility and allows the particles to behave more like hard spheres.

As the volume fraction of hard spheres increases, the equilibrium phase changes from a disordered fluid, to coexistence with a crystalline phase, then to fully crystalline, and finally to a glass. The transition from fluid to crystal requires both the thermodynamic driving force and Brownian motion, which controls the rate. Under normal gravity, sedimentation competes with the crystallization process and prevents the realization of a homogeneous equilibrium state. The first observations by Pusey and van Megen [3] with 614-nm-diameter spheres in decalin and carbon disulfide measured the fraction of crystalline phase at various concentrations after two days, asserting that the crystals were fully nucleated and grown but unaffected by gravity. Defining ϕ from the freezing transition yielded a melting transition at $\phi_m=0.535$, compared with the expected value of 0.545 [9], and $L\sim20$ nm. Paulin and Ackerson [5], on the other hand, constructed the phase diagram by observing the sedimentation of 990-nm-diameter spheres in decalin and tetralin at concentrations in the coexistence region. Crystallites nucleated and grew while settling along with particles in the fluid phase, causing the boundary between pure fluid and the region containing crystallites to first fall rapidly and then rise slowly and linearly with time. Extrapolation of this linear asymptote back to zero time then determined the apparent fraction of the crystalline phase, presumably before individual particles settled but after the crystalline phase equilibrated with the fluid. Paulin and Ackerson also set the hard sphere volume fraction from the freezing transition and found $\phi_m=0.552$ and $L\sim6$ nm. Though extraction of the crystal fraction may be somewhat ambiguous in both cases, the results conform reasonably well with expectations.

In detailed rheological measurements with the PMMA-PHSA dispersions, Mewis *et al.* [6] investigated the effects of ''softness'' with spheres of diameters ranging from 180 to 1220 nm. Measurements of the intrinsic viscosity yielded $L\sim9\pm1$ nm, consistent with previously published data [10]. For the smallest particles with $a/L\sim5$, the high and low shear viscosities diverge at a higher ϕ than for hard spheres; whereas for the particles with $a/L\sim30$ and 61, the high and low shear viscosities diverge at lower ϕ. The deviations from the hard sphere response for the smaller particles clearly arises from the deformability or compressibility of the polymer layer. Increasing either the concentration or the shear rate deforms the layer and reduces the effective volume fraction to a degree that varies with a/L. Thus, as the ratio of particle radius to layer thickness increases, the particles conform more closely to true hard spheres both thermodynamically and hydrodynamically. More recent measurements [11] demonstrate that fixing ϕ from the freezing transition brings the low shear viscosities closer to, but still somewhat above, the data on other hard sphere systems. de Schepper, Cohen, and Verberg [12] suggested considering the effect of polydispersity,

$$\delta=\frac{\sqrt{\overline{a^2}-\overline{a}^2}}{\overline{a}}, \tag{2}$$

since molecular dynamics simulations and density functional theory indicate that the coexistence region narrows and the freezing transition shifts to higher volume fractions ($\phi_f>0.494$) with increasing polydispersity. The critical polydispersity δ_c at which the suspension no longer crystallizes varies, with Moriguchi, Kawasaki, and Kawakatsu [13] and Dickinson and Parker [14] finding $\delta_c\sim0.06-0.07$ and 0.113, respectively, from molecular dynamics simulations, while McRae and Haymet [15] and Barrat and Hansen [16] predicted $\delta_c\sim0.05$ and 0.06–0.07, respectively, with density functional theory. Bolhuis and Kofke [17] performed Monte Carlo simulations on near-Gaussian size distribution of hard spheres, allowing for fractionation, and found $\delta_c=0.057$ for the solid and 0.118 for the fluid. Pusey [18] developed a simple theory based on Lindemann's melting criterion, and found that $\delta_c\sim0.10$. On the experimental side, Underwood, Taylor, and van Megen [19] reported that PMMA-PHSA spheres with $\delta\sim0.10$ showed a disorder-order transition similar to that predicted for monodisperse hard spheres.

Bartlett and Pusey [20] reported that PMMA-PHSA with $\delta_c \sim 0.075$ crystallized slowly in the coexistence region, but samples with concentrations above the melting transition did not crystallize, while for $\delta_c > 0.12$ crystallization did not appear for several months.

Our suspensions have a polydispersity of 0.05 and clearly crystallize. To account for polydispersity, we rescale our core volume fractions according to Bolhuis and Kofke's predictions that $\phi_f = 0.505$ at $\delta = 0.05$, i.e., so that the freezing transition occurs at 0.505. Bolhuis and Kofke also predict that the melting transition moves to $\phi_m = 0.555$ at $\delta = 0.05$.

Our goal is to characterize fully the behavior of monodisperse PMMA-PHSA dispersions with $a/L > 25$ by measuring the phase transition, equation of state, and viscosity, and comparing the results with the hard sphere model. In addition to conventional observations of coexisting phases, we use x-ray densitometry and Zimm viscometry to determine the osmotic pressure and the high and low shear limiting viscosities, respectively.

II. SAMPLE DESCRIPTION

Professor R. H. Ottewill and his group at Bristol University synthesized the PMMA-PHSA particles and determined average core diameters of $2a = 518$ and 640 nm via transmission electron microscopy (TEM). We disperse the PMMA-PHSA particles (bulk $n = 1.503$) in two different media. The first consists of only 1,2,3,4-*cis/trans*-decahydronapthalene (decalin, $n = 1.4750$), which produces an opaque whitish dispersion. For the second, we nearly match the refractive index of the swollen PMMA with that of the medium by mixing *cis/trans*-decalin and 1,2,3,4-tetrahydronapthalene (tetralin, $n = 1.5410$), which bracket the particle refractive index. Tetralin is a good solvent for PMMA and swells the particles, significantly increasing the size [21]. Matching then becomes a dynamic process, so we hasten the equilibration by heating the particles for two hours at 80 °C and adjusting the composition until the cooled suspension does not multiple scatter, which occurs at 55-wt % tetralin with $n = 1.511$ at the sodium *d* line at 20 °C. Since the particles experience similar temperatures during synthesis [7,22], their structure and physical properties should be unaffected aside from the swelling. Index matching prevents multiple scattering, suppresses van der Waals forces, and results in a purplish transparent suspension.

We determine the weight concentrations of our dispersions and then convert to effective volume fractions by constructing the phase diagram and measuring the densities and refractive indices of the PMMA and solvent. The mass of PMMA is determined by drying the suspension in a vacuum oven at 60 °C over two weeks, with the assumption that drying removes the bulk solvent and the tetralin that swells the particles. The weight fraction of PMMA follows as

$$w = \frac{m_{\mathrm{PMMA}}}{m_{\mathrm{PMMA}} + m_t + m_s}, \tag{3}$$

and, assuming that the PHSA layer contributes little to the particle mass, the core volume fraction is

$$\phi_c = \frac{m_{\mathrm{PMMA}}/\rho_{\mathrm{PMMA}} + m_t/\rho_t + \nu_{\mathrm{free}}^{D/M}}{m_{\mathrm{PMMA}}/\rho_{\mathrm{PMMA}} + m_t/\rho_t + m_s/\rho_s + \nu_{\mathrm{free}}^{D/M}}, \tag{4}$$

where m_{PMMA} and ρ_{PMMA}, m_t and ρ_t, and m_s and ρ_s are the mass and bulk density of PMMA, tetralin in the particle, and the solvent, respectively, and ν_{free} is the free volume within the particles. The free volume may be different for PMMA in the two solvents; therefore, a superscript *D* or *M* denotes the free volume of PMMA in decalin or in the index matching mixture, respectively. The effective volume fraction then follows from multiplication by the volume of the core plus polymer layer divided by that of the core alone. The conversion is straightforward for the decalin samples, but must account for the swelling of particles in the index-matching mixture.

With a Mettler-Paar DMA 45 digital density meter, we determined the solvent densities for *cis/trans*-decalin, 0.8779 g/cm^3 at 20 °C and 0.8749 g/cm^3 at 25 °C, for tetralin, 0.9709 g/cm^3 at 20 °C and 0.9678 g/cm^3 at 25 °C, and for the index matching mixture, 0.9282 g/cm^3 at 20 °C and 0.9252 g/cm^3 at 25 °C. A density gradient column, prepared with NaBr and water so that the density varies linearly with height, detects the bulk polymer density. The polymers are heated overnight in a vacuum oven above the glass transition temperature of PMMA (115 °C) to eliminate dissolved solvent or air bubbles trapped inside the polymer. Two samples of PMMA, from decalin and the mixture, yielded densities at 23 °C of 1.1912 and 1.1925 g/cm^3, respectively, indicating that no tetralin remains trapped in the polymer.

Since the density of the bulk PMMA differs from that of the PMMA particles in the solvent, we also measured the total density of the suspension at several volume fractions. From this we could extract the density of the PMMA particles in the solvent. With free volume and/or swelling of the particles by tetralin, the density of the dispersion ρ is

$$\frac{\rho_s}{\rho} = 1 + w\left\{\frac{\rho_t + f(\rho_s - \rho_t)}{\rho_{\mathrm{PMMA}}}\left(1 + \frac{\rho_{\mathrm{PMMA}}\nu_{\mathrm{free}}^{D/M}}{m_{\mathrm{PMMA}}}\right) - 1\right\}, \tag{5}$$

with the degree of swelling

$$f = \frac{m_{\mathrm{PMMA}}/\rho_{\mathrm{PMMA}} + m_t/\rho_t + \nu_{\mathrm{free}}^{D/M}}{m_{\mathrm{PMMA}}/\rho_{\mathrm{PMMA}} + \nu_{\mathrm{free}}^{D/M}}. \tag{6}$$

After some rearranging, the core volume fraction takes the form

$$\phi_c = \frac{f}{f + \dfrac{\rho_{\mathrm{PMMA}}}{\rho_s(1 + \rho_{\mathrm{PMMA}}\nu_{\mathrm{free}}^{D/M}/m_{\mathrm{PMMA}})}\left(\dfrac{1}{w} - 1\right) - \dfrac{\rho_t}{\rho_s}(f-1)}, \tag{7}$$

and the particle density

$$\rho_p = \frac{\rho_{\mathrm{PMMA}}}{f(1 + \rho_{\mathrm{PMMA}}\nu_{\mathrm{free}}^{D/M}/m_{\mathrm{PMMA}})} + \frac{(f-1)}{f}\rho_t. \tag{8}$$

For the dispersions in decalin, $f = 1$ and $\rho_p = 1.166 \pm 0.005$ g/cm^3, indicating $\rho_{\mathrm{PMMA}}\nu_{\mathrm{free}}^{D}/m_{\mathrm{PMMA}} = 0.0224 \pm 0.002$. The density measurements in the index matching mixture do not completely specify the particle density or core volume frac-

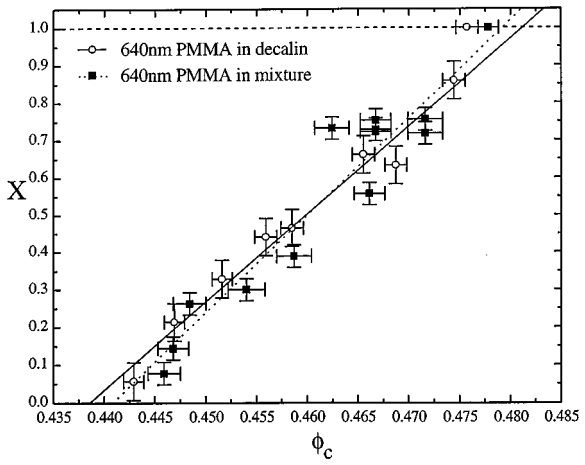

FIG. 2. Phase diagram for 640-nm-diameter PMMA-PHSA spheres in decalin and the index matching mixture gives a layer thickness of 15.1 nm. The solid line represents a linear regression of the decalin data, and the dotted line a linear regression of the index matching mixture data.

tion, because the free volume is unknown. If the free volume remains as in decalin, $\rho_p = 1.087$ g/cm^3 with $f = 1.67$, while, if the free volume is zero, $\rho_p = 1.155$ g/cm^3 with $f = 1.20$. The actual swollen particle density in the index matching mixture probably lies in between the two limits.

Information on the refractive indices at the sodium d line at 20 °C (Abbe refractometer model 2WAJ) complements the density measurements to provide unambiguous estimates of f and ν_{free}^M for the swollen particles in the index matching mixture. Assuming mixing at constant density leads to the refractive index of the swollen particle at the match point as

$$n_s = \frac{n_{\text{PMMA}}}{f} + \frac{n_t(f-1)}{f} + \frac{(1-n_{\text{PMMA}})}{f}\left(\frac{\rho_{\text{PMMA}}\nu_{\text{free}}^{D/M}/m_{\text{PMMA}}}{\rho_{\text{PMMA}}\nu_{\text{free}}^{D/M}/m_{\text{PMMA}}+1}\right), \quad (9)$$

where the subscripts are as before. With the measured values of the refractive indices of the individual components and the index matching mixture cited above, we find that $f = 1.63$ if the free volume remains as in decalin, and $f = 1.26$ if the free volume is zero. Requiring Eqs. (5) and (9) to conform with experimental values yields $f = 1.29 \pm 0.05$ and $\rho_{\text{PMMA}}\nu_{\text{free}}^M/m_{\text{PMMA}} = 0.002$. Thus, in the index matching mixture samples, the tetralin appears to occupy most of the free volume.

To estimate the layer thickness and confirm the degree of swelling, we constructed the phase diagram by observing the sedimentation of PMMA dispersions at various core volume fractions [5] in glass vials sealed with a teflon lined cap and teflon tape at room temperature (21±1 °C). Within a few weeks the samples separate into three distinct layers with the crystalline solid at the bottom, a clear supernatant on top, and a fluid dispersion in between. As the fluid phase settled and the crystalline layer grew, the height of each layer was carefully measured with a cathetometer. The phase diagrams for dispersions in both pure decalin and the index matching mixture shown in Fig. 2 were constructed by extrapolating the position of the crystalline-fluid interface to zero time. We choose the scale factor between the swollen core and hard sphere volume fractions such that $\phi = 0.505$ at the core volume fraction where crystals begin to form. For the decalin samples this translates into $L = 15.1 \pm 1.5$ nm and $f = 1$ with $\phi_m = 0.552 \pm 0.005$. For the index matching mixture we assume $L = 15.1 \pm 1.5$ nm as well, and determine from the phase diagram and density measurements that tetralin swells the core radius by 26.0±3.0 nm or $f = 1.263$. The melting transition in the mixture occurs at $\phi_m = 0.544 \pm 0.008$.

Both values for the melting transition closely correspond to the theoretical value for polydisperse hard spheres of $\phi_m = 0.555$. Table I summarizes the diameters determined from the various methods. The apparent diameters from the phase diagram are consistent with our dynamic light scattering results, which give hydrodynamic diameters of 668±16 nm in decalin and 716±20 nm in the index matching mixture. The hydrodynamic size for the swollen spheres in the index matching mixture corresponds to $f = 1.28 \pm 0.11$ with $\nu_{\text{free}}^M/m_{\text{PMMA}} \sim 0$ as compared with $f = 1.29 \pm 0.05$ deduced from the measurements of physical properties above. Thus we conclude that the volume change upon mixing of tetralin in PMMA is slightly negative, and that accounting for that effect provides reasonable consistency among the measurements of density, refractive index, and hydrodynamic and thermodynamic radii. In addition, the volume fractions at freezing and melting are within experimental error of those expected for hard spheres, as asserted by previous investigators [3,5].

III. X-RAY DENSITOMETRY

The deviation of the osmotic pressure

$$\Pi(\phi) = nkTZ(\phi) \quad (10)$$

from the ideal, dilute limit is expressed in Z, the compressibility factor. For the fluid state, Carnahan and Starling [23] formulated the approximation

$$Z_{\text{fluid}}(\phi) = \frac{1+\phi+\phi^2-\phi^3}{(1-\phi)^3} \quad (11)$$

to capture the first seven virial coefficients and available results from computer simulations. For a face-centered-cubic crystal, Hall [24] constructed a modified Padé approximant from results from computer simulations in the form

$$Z_{\text{solid}}(\phi) = \frac{12-3\beta}{\beta} + 2.557\,696 + 0.125\,307\,7\beta + 0.176\,239\,3\beta^2 - 1.053\,308\beta^3 + 2.818\,621\beta^4 - 2.921\,934\beta^5 + 1.118\,413\beta^6, \quad (12)$$

with $\beta = 4(1-\phi/\phi_{\max})$ and $\phi_{\max} = 0.74$.

TABLE I. Summary of the PMMA particle sizes in both pure decalin and the index matching mixture, where a is the radius and L the polymeric layer thickness, obtained by several methods. The first column represents the unswollen TEM diameter. The particle sizes for PMMA in the index matching mixture determined from the total suspension density-refractive index, the total suspension density-phase diagram, dynamic light scattering (DLS), and equation of state (EOS) all refer to the swollen diameters.

		$2a$ (nm)		$2(a+L)$ (nm)		
Particle size technique		TEM	density+n_D	density plus phase diagram	DLS	EOS
PMMA	in decalin	640±30	NA	670±3	668±16	681±8
PMMA	in mixture	640±30	697±9	722±9	716±20	723±6

To test how well the PMMA-PHSA system conforms to these predictions, we scan an equilibrium sediment with an x-ray microdensitometer, thereby achieving a more sensitive measure of the osmotic pressure than with the compression cell of Cairns *et al.* [7]. The volume fraction profile in an equilibrium sediment reflects the balance between gravitational forces and the osmotic pressure gradient. Integration of this balance from the upper surface to any depth h determines the osmotic pressure as the total weight of the overlying particles,

$$\Pi(h)=\int_h^\infty g\Delta\rho\phi_c(z)dz, \tag{13}$$

where $\Delta\rho$ is the density difference between the particle and solvent. We can integrate the volume fraction profile numerically to obtain the osmotic pressure as a function of volume fraction for comparison with the Carnahan-Starling and Hall equations. However, the densitometry must resolve the rapid change in volume fraction at the top of the sediment.

In an equilibrium sediment, the phase transition should appear as a discontinuity in the volume fraction, as the pressure is constant. On either side of this discontinuity the derivative of Eq. (13) with respect to the volume fraction gives

$$\frac{d\phi(z)}{dz}=-\phi(z)\,\frac{\kappa_T}{l_0}, \tag{14}$$

where the compressibility is $\kappa_T=kT\nu_p(d\Pi/d\phi)^{-1}$, the gravitational height is $l_0=kT/(\Delta\rho g\nu_p)$, and $\nu_p=4\pi a^3/3$ is the particle volume. For an ideal gas, the solution to Eq. (14) produces the law of atmospheres with the gravitational height appearing in the exponent and reflecting a balance between Brownian motion, which tends to disperse, and gravity, which draws the particles downward. For our smaller particles, the gravitational height is on the order of 20 μm at infinite dilution and increases with volume fraction as

$$\frac{l(\phi)}{l_0}=\frac{4\pi a^3}{3kT}\,\frac{d\Pi}{d\phi}. \tag{15}$$

Thus at the phase transition $l(\phi)\sim 30l_0$. For the larger particles, $l_0=15$ μm at infinite dilution.

Piazza, Bellini, and Degiorgio [25] measured the equation of state of an equilibrium sediment of hard spheres by depolarized light scattering, but, at high volume fractions, found the osmotic pressure to deviate from ideal crystal behavior, possibly due to an electrostatic effect in their screened charged colloids. Rutgers *et al.* [26] demonstrated that x-ray densitometry with a two-dimensional area detector can accurately measure the equation of state. This technique is nondestructive, averages over most of the cross section, and scans all heights with one exposure to eliminate any noise due to instrument drift. Beer's law, which relates the attenuation of the x-ray intensity I/I_0 to the thickness x and absorption coefficient $1/\xi$ of the sample as

$$I=I_0\,\exp(-x/\xi), \tag{16}$$

permits an intensity profile to be converted to a volume fraction profile. For all images, we first subtract the dark counts D and then normalize with an image of a cell filled only with the solvent according to

$$I_N=\frac{I-D}{I_s-D}=\exp[-x\phi\Delta\xi^{-1}], \tag{17}$$

where $\phi\Delta\xi^{-1}=(\xi^{-1}-\xi_s^{-1})$, and the subscript s refers to the solvent. This normalization, performed pixel by pixel, should remove nonuniformities due to the incident beam, imperfections in the scintillator crystal, and the slight vertical tapering in the PMMA cuvettes.

Figure 3 shows the essential components of the x-ray setup, which are placed on an optical table enclosed by a leaded plexiglass hutch. A 35-keV electron beam at 40 mA excites a molybdenum target to produce a characteristic emission at 17.444 keV with a Bremsstrahlung tail. A zirconium foil filters out most of the tail. The beam then passes through a lead mask that defines the area of interest within the sample. A scintillator crystal right behind the sample converts the transmitted x-rays to visible light. A lens focuses the light onto a cooled charge coupling device chip (TK1024a), which captures it as a 1024×1024-pixel image.

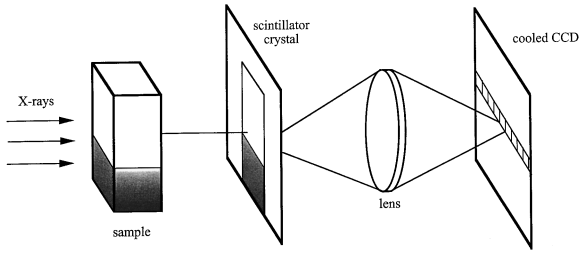

FIG. 3. Essential components of the x-ray microdensitometry setup.

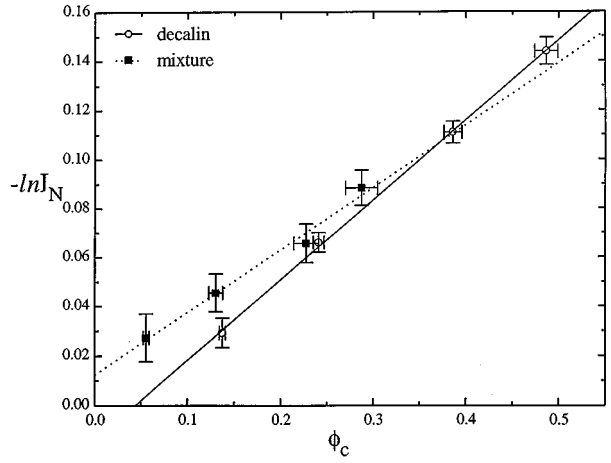

FIG. 4. Calibration of normalized x-ray intensity with unswollen ϕ_c, calculated from suspension density and phase diagram measurements, results in $\Delta\xi^{-1}=0.326\pm0.01$ and 0.254 ± 0.02 cm^{-1} for decalin and the index matching mixture, respectively.

To reduce the effect of smearing, the upper interface of the sediment is aligned to the medial plane; thus the image only captures 3 mm of the sediment. Smearing results because the source is not a point but rather a 0.5×0.8-mm^2 rectangle at a finite distance, approximately 1 m from the samples. This results in an 6.0-μm pixel spatial resolution in the sample, which suffices to resolve the density profile from the dilute gas phase, a millimeter above the phase transition, to volume fractions approaching close packing, a few millimeters below the phase transition. This will be evident in the equation of state, which we show later.

Samples are stored in standard poly (methyl methacrylate) spectrophotometry cells sealed with Duco cement, tapered teflon caps, and telfon tape, and left to settle completely within a styrofoam box that damps any rapid temperature fluctuations in the room. An estimate based on the densities of all constituent elements with linear interpolation of the x-ray mass absorption coefficients given in International Tables of Crystallography for 17.4 keV puts the absorption coefficient for PMMA $[\text{-}CH_2C(CH_3)(CO_2CH_3)\text{-}]_n$ at 0.8826 cm^{-1}, for the decalin ($C_{10}H_{18}$) at 0.623 cm^{-1}, and for the index matching mixture ($C_{10}H_{12}+C_{10}H_{18}$) at 0.630 cm^{-1}. These values indicate that the signal should be detectable with sufficient contrast to obtain good intensity profiles. We calibrate the absorption coefficients by imaging four samples in each dispersion medium with unswollen core volume fractions. Their images were normalized and averaged to obtain the results shown in Fig. 4. The corresponding differences in absorption coefficients between the particle and media are $\Delta\xi^{-1}=0.326\pm0.01$ cm^{-1} for the decalin and $\Delta\xi^{-1}=0.254\pm0.02$ cm^{-1} for the index matching mixture, compared with the values from the International Tables of 0.260 cm^{-1} for the decalin samples and 0.253 cm^{-1} without swelling for the index matching mixture. The measured and calculated values do not agree exactly, because the x rays are not perfectly monochromatic and the sample composition is not known exactly.

At low concentrations, we expect the volume fraction to decrease exponentially with height according to Eq. (13), but deficiencies in the imaging system produce instead a very long tail at the top of the bed, as found by Rutgers *et al.* To determine if the long tail is real [27], we imaged a 0.4-mm piece of aluminum across a cell filled with index matching mixture. The aluminum has a similar contrast ($I_N=0.924$) to our samples ($0.92>I_N>0.86$). Perfect imaging would generate a sharp discontinuity, but instead the edge is smeared across approximately four pixels. The line spread function is the derivative of the edge. If the edge is horizontal, the row sum of the line spread function gives the point spread function (PSF), the Fourier transform of which is the modulation transfer function (MTF). We divide the Fourier transform of the data by the MTF and then invert the Fourier transform to filter the data. A perfect imaging system would give the same image contrast at all spatial frequencies. Our somewhat Gaussian PSF causes decreasing contrast at higher spatial frequencies, so filtering our images with the MFT would amplify the suppressed high spatial frequencies as well as the noise. Since our intensity profiles are gradual, the higher spatial frequencies contain little information, so we reduce the noise introduced by filtering by cutting off our MTF at high spatial frequencies, thereby removing much of the long tail while leaving the rest of the profile unchanged except for some noise.

Equation of state

We prepared four samples at $\phi_0\sim0.20$ to achieve a 1.0-cm sediment height: 518-nm PMMA in decalin and in the index matching mixture and 640 nm in decalin and in the index matching mixture. To estimate the time required for the dispersions to settle completely, we refer to the sedimentation velocities reported by Paulin and Ackerson [5] for PMMA spheres as a function of volume fraction, as reduced with the Stokes settling velocity of a single particle,

$$U_0=\frac{2a^2g\Delta\rho}{9\mu}, \tag{18}$$

where μ is the medium viscosity. Dispersions initially at concentrations below the freezing transition settle with three distinct regions: freely settling, transition and sediment [28]. For our particular system, where the suspension is relatively monodisperse and sedimentation is slow, an ordered sediment accumulates at a rate, $\phi^+U(\phi^+)/(\phi_{\max}-\phi^+)$ proportional to the sedimentation velocity, $U(\phi^+)$, of the fluid just above the sediment. Thus the time for sediment formation is the final height $H\phi_0/\phi_{\max}$ divided by the rate of accumulation, i.e.,

$$t_{\text{set}}=\frac{H}{U(\phi^+)}\frac{\phi_0}{\phi^+}\left(1-\frac{\phi^+}{\phi_{\max}}\right) \tag{19}$$

[28], where $\phi^+\sim0.505$, $\phi_{\max}\sim0.6$–0.7, and $U(\phi^+)=0.016U_0$ [5]. Therefore, the 640-nm particles should require about one month to settle, and the 518-nm particles about two months, but the sediment may take considerably longer to equilibrate fully.

After six months, all samples settled completely into an opalescent, crystalline sediment with clear fluid above. Only the 518-nm PMMA samples had a disordered layer visible to the eye. Samples were carefully positioned with the medial plane at the interface between fluid and crystal to reduce

TABLE II. Summary of the effective x-ray-absorption coefficient differences between PMMA and the solvent, and their corresponding melting transitions determined from x-ray densitometry as well as from constructing the phase diagram. In both measurements, we set the freezing transition for polydisperse hard spheres at $\phi_f = 0.505$.

	$\Delta\xi^{-1^*}[a/(a+L)]^3$ (cm^{-1})	ϕ_m
phase diagram		
640 nm in decalin	NA	0.552± 0.005
in mixture	NA	0.544±0.008
x-ray densitometry		
518 nm in decalin	0.274 ± 0.002	0.555± 0.004
in mixture	0.223±0.003	0.552±0.005
x-ray densitometry		
640 nm in decalin	0.281 ± 0.003	0.562± 0.007
in mixture	0.232±0.003	0.557±0.007

smearing and exposed for 180 s. The images were normalized and averaged in the direction perpendicular to gravity to obtain an intensity profile. The phase transition is apparent with both the 518- and 640-nm PMMA particles.

We integrate the profiles to calculate the osmotic pressure and choose the effective calibration constant or $\Delta\xi^{-1^*}[a/(a+L)]^3$ to match the freezing transition at $\phi = 0.505$. Comparing the effective calibration constant with the $\Delta\xi^{-1}$ extracted from the core calibration for the 640-nm particles suggests $L = 20.9 \pm 4.0$ nm for decalin and 15.3 ± 3.0 nm for index matching mixture without swelling. The layer thickness for the decalin sample is consistent with other published data on PMMA particles, which range from 6 nm [5] to 20 nm [3], but a bit thicker than that obtained from our phase diagram. The discrepancy may result from errors in determining the core volume fraction for the calibration samples and nonuniformities in the PMMA cuvettes. The corresponding melting transition for the 518- and 640-nm PMMA in both solvents occurs within 0.007 of the theoretical value for polydisperse hard spheres of $\phi_m = 0.555$. Table II summarizes the calibration constants obtained by matching the polydisperse hard sphere freezing transition and the corresponding melting transitions for all four samples as well as the phase diagram results.

To obtain the osmotic pressure in accord with Eq. (13), we integrated the unfiltered data from $\phi \sim 0.05$, where the smearing does not affect the profile, and added a constant to account for the smearing by matching the pressure to the Carnahan-Starling equation. Figure 5 shows the results with the data for the smaller particles offset to illustrate the trends clearly. For each particle size, the data superimpose for the decalin and the index matching mixture. For all samples, the pressure in the fluid phase matches the Carnahan-Starling equation, but the pressure in the crystal exceeds the Hall equation, diverging at $\phi_{\max} \sim 0.725$ instead of 0.74, perhaps due to a direct effect of polydispersity.

The pressure in the solid phase extracted from similar measurements for essentially hard sphere polystyrene in water by Rutgers *et al.* [26] matches the Hall equation almost exactly. Their sediments exhibit columnar iridescence, with a length scale of roughly 1 mm, indicating much larger crystallites than ours. Thus a plausible explanation for the higher pressure in the crystalline phase is polycrystallinity or defects and/or grain boundaries. Suppose, for example, that crystallites of volume V with radii R and internal volume fraction ϕ_s have an interfacial region of thickness $\sim a$ and

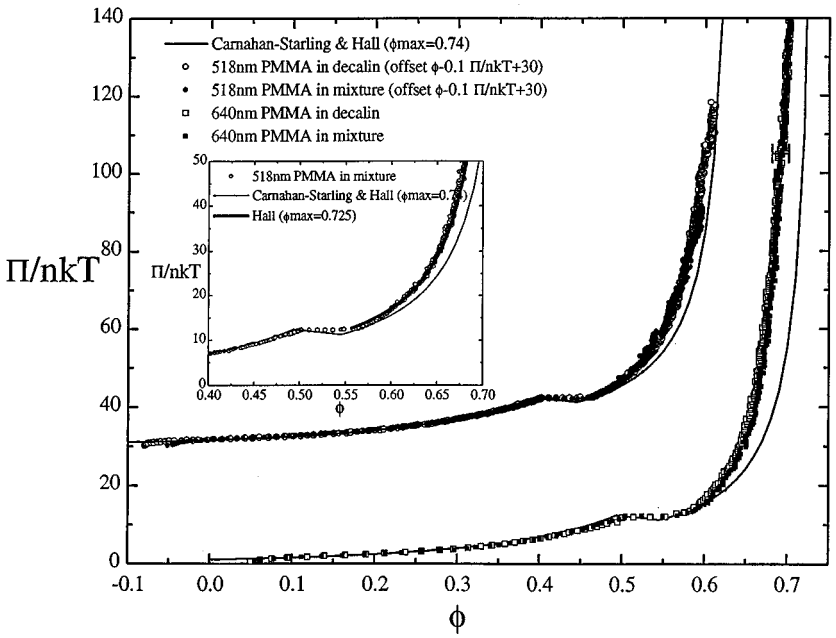

FIG. 5. Equation of state for 518- (offset by $\phi - 0.1$, $\Pi/nkT + 30$) and 640-nm-diameter PMMA-PHSA particles in both decalin and the index matching mixture. We set the freezing transition to that expected for slightly polydisperse hard spheres, i.e., $\phi_f = 0.5051$. The solid line refers to the Carnahan-Starling and Hall expressions with $\phi_{\max} = 0.74$. Inset: Magnification of the equation of state for 518-nm-diameter PMMA-PHSA in the index matching mixture. The thicker solid line refers to the Hall expression with $\phi_{\max} = 0.725$.

interfacial area A. Forces must balance across the disordered interfacial region, causing the overall volume fraction to be lower than the ϕ_s associated with the pressure, e.g.,

$$\phi = \frac{V\phi_s + aA\phi_d}{V + aA} \approx \frac{\phi_s + \frac{3a}{R}\,\phi_d}{1 + \frac{3a}{R}}, \tag{20}$$

where ϕ_d, the volume fraction of the disordered region, is set by mechanical equilibrium, $\Pi(\phi_s) = \Pi(\phi_d)$. Figure 5 indicates $(0.74 - \phi_{\max}) \sim 0.015$–$0.02$, which means that $R \sim 12a$ for the 640-nm-diameter PMMA spheres and $R \sim 17a$ for the 518-nm-diameter PMMA spheres would be required to rationalize the data with $\phi_d = 0.64$. Though possible, this would imply rather small crystallites. On the other hand, crystallites might contact adjacent crystallites directly without particles in between, i.e., $\phi_d = 0$. In this case, $R \sim 108a$ for the 640-nm-diameter PMMA spheres and $R \sim 145a$ for the 518-nm-diameter PMMA spheres would rationalize the data. These crystallite sizes are reasonable since our samples have visible but small grains (<1 mm). We conclude that polycrystallity may distinguish our pressures from those of Rutgers *et al.* or a perfect fcc solid. The crystallite size most likely lies between the two cases analyzed above.

IV. ZIMM VISCOMETRY

Typical viscosity vs shear rate curves for hard sphere fluids show Newtonian plateaus at high and low shear rates separated by a shear thinning region. The high shear viscosity η_∞ derives from hydrodynamic forces with a structure displaced far from equilibrium, and the low shear viscosity $\eta_0 > \eta_\infty$ includes contributions from hydrodynamic forces associated with the equilibrium structure as well as from interparticle and Brownian forces for a structure slightly perturbed from equilibrium [28,29]. In general, if one plots the inverse of the square root of the limiting steady shear viscosities versus volume fraction, extrapolation identifies the $\phi_{\max}$ at which the curves apparently diverge. For polymerically stabilized spheres, these values then characterize the softness of the stabilizing layer and/or the nature of the microstructure at high and low shear [6]. Normally, the low shear limit apparently diverges at a lower volume fraction than the high shear limit, with the former generally corresponding to random close packing and the latter suggesting that spheres in hexagonal layers slide over each other in a zigzag pattern.

In the dilute limit where pairwise interactions dominate, Batchelor [30] calculated the low shear viscosity from a numerical solution of the equation governing the perturbation of the microstructure, obtaining far-field $(2.5\phi^2)$ and near-field $(2.7\phi^2)$ hydrodynamic contributions plus that from Brownian motion $(1.0\phi^2)$, such that

$$\eta_0/\mu = 1 + 2.5\phi + 6.2\phi^2 + O(\phi^3). \tag{21}$$

The interparticle forces do not contribute because hard spheres repel each other only at contact where the hydrodynamic mobility goes to zero. Experiments on hard spheres follow [31]

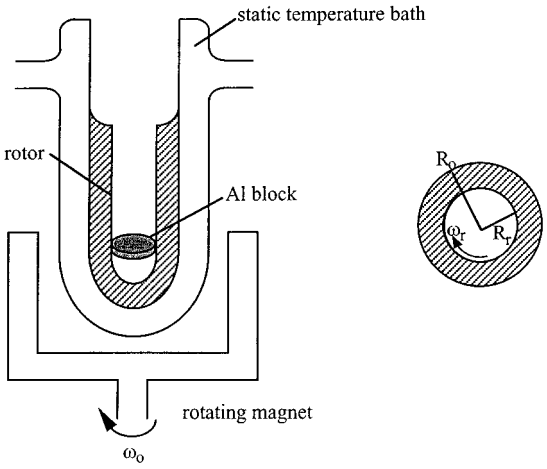

FIG. 6. Diagram of the Zimm viscometer.

$$\eta_0/\mu = 1 + 2.5\phi + (4 \pm 2)\phi^2 + (42 \pm 10)\phi^3,$$
$$\eta_\infty/\mu = 1 + 2.5\phi + (4 \pm 2)\phi^2 + (25 \pm 7)\phi^3 \tag{22}$$

in the dilute limit, and

$$\eta_0/\mu = (1 - \phi/\phi_{\max})^{-2} \tag{23}$$

at higher volume fractions, with $\phi_{\max} = 0.63 \pm 0.02$ for low shear and $\phi_{\max} = 0.70 \pm 0.02$ for high shear. The critical stress associated with shear thinning is of order

$$\sigma_c \approx \frac{kT}{a^3}, \tag{24}$$

but shifts to lower values at $\phi > 0.5$. Thus the Newtonian low shear regime lies at stresses more than an order of magnitude below the critical stress and the Newtonian high shear regime at $\sigma \gg \sigma_c$.

A Zimm viscometer covers a wide range of shear stresses (10^{-5}–1 Pa), and can detect shear rates as low as $10^{-5}\ \mathrm{s}^{-1}$ to obtain these limiting viscosities [32,33]. The viscometer pictured in Fig. 6 consists of a temperature-controlled static outer cylinder of radius R_0 filled with the fluid of interest, and a freely floating rotor of radius R_r supported by its own buoyancy and held in place by fluid surface tension. A constant torque is applied by the interactions of an aluminum block sitting at the bottom of the rotor with an applied rotating magnetic field. A HP3325*A* synthesizer–function generator and pulse motor drive the magnet at a constant but adjustable angular velocity. Thus a constant shear stress is applied to the fluid between the cylinders. The inner rotation rate is determined by reflecting a laser beam from a circle of alternating black and reflective radial stripes on top of the aluminum block. As the rotor turns the reflection of the beam from a point off the center of the circle blinks on and off. The beam impinges on a photodiode, an analog to digital card converts the signal, and this oscillating digitized signal determines the frequency. Equating the magnetically induced torque to the viscous torque on the rotor determines the steady shear viscosity η in terms of the rotor and motor rotation rates ω_r and ω_m, respectively, as

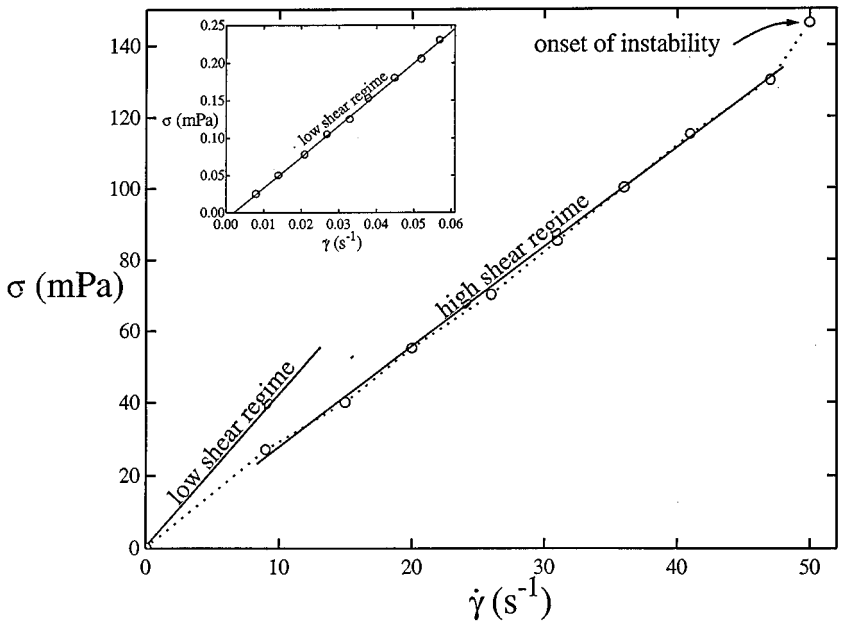

FIG. 7. Typical stress vs shear rate curve for our dispersion. Inset: Magnification of the low shear regime.

$$\eta = C\,\frac{\omega_m - \omega_r}{\omega_r}. \tag{25}$$

The calibration constant C depends on the strength of the magnetic field and the conductivity and size of the aluminum block. The average shear rate within the annular gap is

$$\langle \dot{\gamma} \rangle = \frac{4R_0^2 R_r^2 \,\ln(R_0/R_r)}{R_0^2 - R_r^2}\,\omega_r, \tag{26}$$

and the average stress follows as

$$\langle \sigma \rangle = \eta \langle \dot{\gamma} \rangle = C\,\frac{4R_0^2 R_r^2 \,\ln(R_0/R_r)}{R_0^2 - R_r^2}\,(\omega_m - \omega_r). \tag{27}$$

At high shear rates, instability becomes a potential problem beyond a Taylor number of [34]

$$T_c \equiv \left[\frac{2R_r^2 \dot{\gamma}_{\rm trans}\rho/\eta}{1-(R_0/R_r)^2}\right]^2 \approx 3416 \tag{28}$$

for a static outer and rotating inner cylinder, causing the stress to increase nonlinearly with shear rate. This sets an upper bound on the shear rates available.

Two separate rotors, aluminum blocks, and magnets are required for the high and low shear rate measurements. We used a ceramic magnet with a strength of 2300–2400 G at low shear rates, and a neodymium iron boron magnet with a strength of 11 000–12 000 G for the high shear. Before calibrating, we determined the optimum vertical position of the rotor associated with the minimum ratio of the magnet frequency to the rotor frequency as a function of volume of fluid. With too little fluid, friction from the bottom of the temperature bath becomes important, while the aluminum block floats out of the magnetic field with too much fluid. Because of the different rotor radii, the optimum volume is 6.4 mL for the high shear rates and 10.5 mL for the low, leaving a 7-mm gap between the bottom of the temperature bath and the bottom of the rotor in both cases. The minimum is rather broad, accommodating ± 0.5 mL in the fluid volume. As the density of the dispersion increases with volume fraction, the mass is adjusted by adding circular plastic pieces that fit snugly into the rotor.

The instrument is calibrated with several Newtonian fluids (water, *trans*-decalin, *cis*-decalin, glycerol, and sucrose solutions) with known viscosities ranging from 1 to 70 m Pa s. Temperature affects the calibration constant slightly but, for the relative viscosities of interest, the calibration constant and, therefore, the temperature dependence cancel. For each volume fraction of our sample, we measure the viscosity at 20 and 25 °C to check that the relative viscosities are invariant. To prevent evaporation for the higher viscosity samples, we seal the temperature bath with some clay and a watch glass. We clean the temperature bath and rotor carefully with ethanol before loading a new sample, and then remove any bubbles that may stick to the wall.

Measurements with either the single phase fluid or at high shear rates proved relatively straightforward, taking roughly 3–4 h to obtain sufficiently reproducible data. In the coexistence region, however, the high viscosities required a couple of weeks at low shear rates, allowing crystallites to settle and phase separate macroscopically. Consequently, the gap between the bottom of the temperature bath and the bottom of the rotor decreases and the additional friction significantly reduces the shear rate. This time dependence plus the inherent ambiguities in seeking a low shear viscosity for a two-phase mixture rendered the measurement infeasible.

Limiting steady shear viscosities

Figure 7 shows a typical stress vs shear rate curve for our

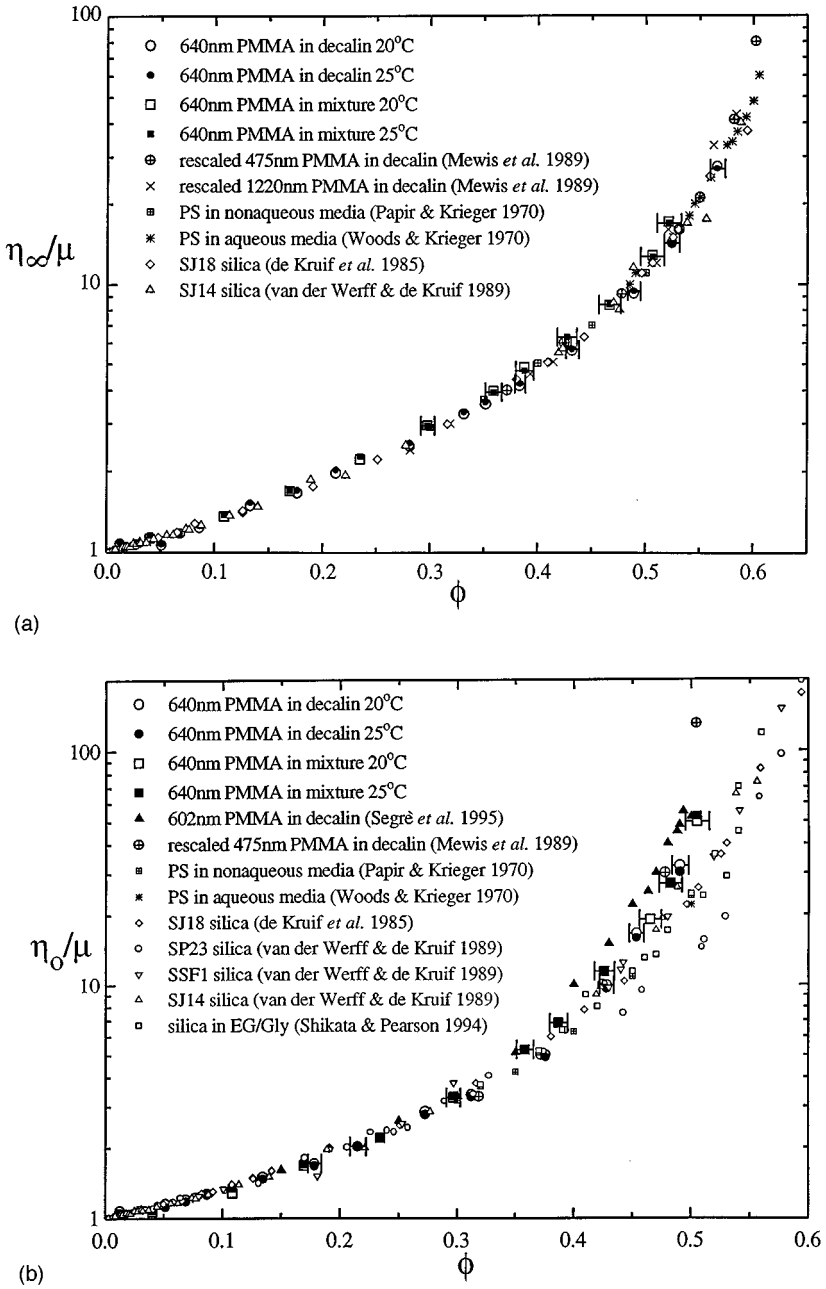

FIG. 8. (a) High shear viscosities and (b) low shear viscosities for 640-nm-diameter PMMA-PHSA spheres, where ϕ is calculated from suspension density and phase diagram measurements with the freezing transition set to that expected for slightly polydisperse hard spheres, i.e., $\phi_f=0.505$, compared with other published hard sphere systems. We rescaled Mewis *et al.*'s [6] volume fractions so that $\eta_\infty/\mu=11.5$ at $\phi=0.50$.

dispersions. The low shear regime generally occurs for $\langle\dot{\gamma}\rangle=10^{-3}-10^{-2}$ s^{-1}, and the high shear regime for $\langle\dot{\gamma}\rangle=1-50$ s^{-1}. The high and low shear viscosities as a function of ϕ, determined from our phase diagram and swelling measurements and shifted to include polydispersity effects, are compared in Figs. 8(a) and 8(b), respectively, with several other sets of published data for hard spheres. For $\phi<0.5$, the measurements are highly reproducible, with an uncertainty of 2.0% for the low shear and 3.0% for the high shear. The error in weight fraction is ±0.003, which translates into ±0.003 in core volume fraction. The effective volume fraction, determined by matching the freezing transition, introduces an additional uncertainty of up to ±0.007 for decalin and ±0.010, for the index matching mixture.

Since the refractive index of the decalin differs from that of the particle, van der Waals attractions might increase the relative low shear viscosities. Estimation of the non retarded limit of the Hamaker constant from

$$A_{\mathrm{eff}}(0)=\tfrac{3}{4}kT\left(\frac{\overline{\varepsilon(0)}-\varepsilon(0)}{\overline{\varepsilon(0)}+\varepsilon(0)}\right)^2+\frac{3h\omega}{32\pi\sqrt{2}}\frac{(\overline{n_0^2}-n_0^2)^2}{(\overline{n_0^2}+n_0^2)^{3/2}} \tag{29}$$

requires Planck's constant h; $\varepsilon(0)$, the dielectric constant at

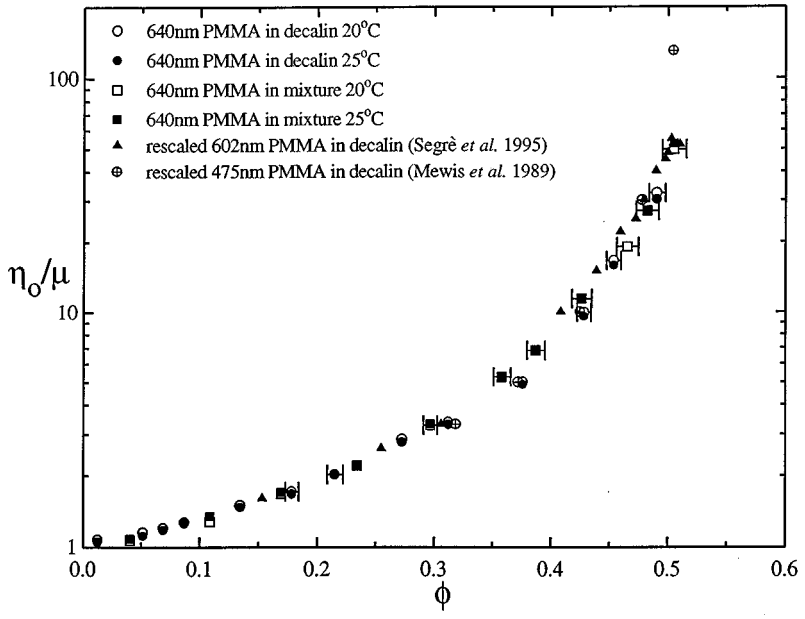

FIG. 9. Low shear viscosities for 640-nm-diameter PMMA-PHSA spheres, where ϕ is calculated from suspension density and phase diagram measurements with the freezing transition set to that expected for slightly polydisperse hard spheres, i.e., $\phi_f=0.505$, compared with other published PMMA-PHSA data. We rescaled Mewis *et al.*'s [6] volume fraction so that $\eta_\infty/\mu=11.5$ at $\phi=0.50$, and Segrè *et al.*'s [11] volume fraction to account for 5% polydispersity.

zero frequency; ω_{uv}, the frequency for the dominant relaxation in the ultraviolet wavelengths; and n_0, the refractive index at the sodium *d* line at 20 °C [28]. Quantities with a bar overhead refer to the particle, and those without to the solvent. Relaxations in the ultraviolet dominate the portion of the dielectric spectra most important for dispersion interactions. Assuming the $\varepsilon(0)$ and ω_{uv} of PMMA to be close to those for polystyrene yields $A_{\rm eff}(0)\approx 0.066kT$, i.e., a very weak attraction, which our measurements support since the low shear viscosities in the mixture and decalin coincide.

Our relative high shear viscosities are consistent up to the freezing transition with those for silica spheres sterically stabilized with octadecyl chains in cyclohexane and polystyrene lattices in water and other polar solvents, despite all the different means for converting weight concentrations to hard sphere volume fractions [Fig. 8(a)]. Papir and Krieger's polystyrene in nonaqueous solvents [35] have standard deviations in diameter less than 5% and an $O(\phi)$ coefficient of 2.67, i.e., close to the Einstein value of 2.5. Their values of $\eta_\infty/\mu=11.5$ for crosslinked polystyrene in benzyl alcohol or *m*-cresol at $\phi=0.50$ compare well with our measurements on PMMA in both decalin and index matching mixture, $\eta_\infty/\mu=11.5$. However, both nonaqueous samples crystallize for $\phi>0.30$, suggesting that the particles may be slightly charged. Woods and Krieger [36] obtained similar results for aqueous dispersions by accounting for a surfactant layer thickness of $L=2.25$ nm in defining the volume fraction as

$$\phi=\phi_c(1+3L/a). \tag{30}$$

This collapses relative high shear viscosities for different particle sizes onto a single curve with $\eta_\infty/\mu=11$ at $\phi=0.50$. de Kruif *et al.* [31] and van der Werff and de Kruif [37] obtained equivalent high shear viscosities for silica spheres, of several different diameters and polydispersity greater than 9%, stabilized sterically with octadecyl chains in cyclohexane. They dried the particles to determine the mass concentration, measured the intrinsic viscosity with a Ubbelohde capillary viscometer, and thereby calculated the volume fraction. Given the larger polydispersity and the uncertainty in measuring intrinsic viscosity, these are the most questionable volume fractions.

Mewis *et al.* [6] followed a similar procedure with 475- and 1220-nm-diameter PMMA-PHSA in Exsol D200/240 and decalin but found $\eta_\infty/\mu=17\pm1.0$ at $\phi=0.50$. The correspondence of our high shear viscosities with the prior measurements for hard sphere dispersions and the deviation of Mewis *et al.* suggest that matching the freezing transition to the hard sphere value may be the proper scaling. Hence, we have ''corrected'' their volume fractions to bring the data for η_∞ into line. Beyond the freezing transition, our relative high shear viscosities in the index matching mixture deviates somewhat, e.g., $\eta_\infty/\mu=17\pm2.0$, relative to Woods and Krieger's value of 14.6 at $\phi=0.52$, but more data points at higher concentrations are needed to be definitive.

In the low shear limit the situation is rather different [Fig. 8(b)], since our viscosities and those reported recently by Segrè *et al.* [11] significantly exceed the values for octadecyl silica spheres in cyclohexane and polystyrene latices in water and other polar solvents. For example, at $\phi=0.50$ Papir and Krieger [35] and Woods and Kreiger [36] measured $\eta_0/\mu=24$ for polystyrene in benzyl alcohol or *m*-cresol and $\eta_0/\mu=22$ for polymer latices in aqueous dispersions, respectively, while van der Werff and de Kruif [37] found values of 13, 21, and 30 for octadecyl silica of three different particle sizes in cyclohexane. Shikata and Pearson [38] found $\eta_0/\mu=25.4$ at $\phi=0.50$ for bare silica particles. Our measurements, as well as those of Segrè *et al.*, on PMMA-PHSA in both decalin and the index matching mixture give higher

values, about $\eta_0/\mu=45\pm3$ for our particles and $\eta_0/\mu=50$ for Segrè *et al.*'s. The data of Mewis *et al.* with the ''corrected'' volume fractions produces $\eta_0/\mu=55\pm10$ at $\phi=0.50$ and $\eta_0/\mu=30\pm5$ at $\phi=0.477$, close to Segrè *et al.*'s data and our own. Finally, applying the 5% polydispersity correction to Segrè *et al.*'s volume fractions shifts their low shear viscosities into reasonably close accord with those from Mewis *et al.* and this paper (Fig. 9). Thus we are left with two bands of data, the higher one for the PMMA-PHSA dispersions, and the lower for the polystyrene and silica systems. Fitting all the PMMA-PHSA low shear viscosities for $0.30<\phi<0.50$ to the Krieger-Dougherty equation

$$\frac{\eta_0}{\mu}=\left(1-\frac{\phi}{\phi_{\max}}\right)^{-2} \tag{31}$$

gives $\phi_{\max}=0.577\pm0.005$.

The different low shear viscosities for the PMMA-PHSA dispersions relative to the polystyrene and octadecyl silicas could reflect fundamental differences. However, complications due to the slight permeability or softness of the PHSA layers, polydispersity in the octadecyl silicas, and molecular level details with the polymer latices may prove difficult to sort out. Since our equation of state measurements indicate that PMMA-PHSA dispersions behave as hard spheres up to $\phi=0.60$, we believe that the PMMA-PHSA data may represent the hard sphere curve for the low shear viscosities.

V. CONCLUSIONS

We convert our core volume fractions to hard sphere volume fractions by matching the freezing transition to that expected for slightly polydisperse hard spheres, $\phi_f=0.505$, thereby obtaining (i) a polymer layer thickness in reasonable accord with other published data on the PMMA-PHSA particles; (ii) a melting transition within experimental uncertainty of that expected for polydisperse hard spheres; (iii) an osmotic pressure in the fluid state that matches the Carnahan-Starling equation and provides the most direct evidence to date that PMMA dispersions with $\phi<0.60$ can be approximated as hard spheres; (iv) high shear viscosities consistent with those from polystyrene and octadecyl silica; and (v) low shear viscosities consistent with other data on the PMMA-PHSA system but significantly higher than for the polystyrene, octadecyl silica, and bare silica. Several means of extracting the hard sphere volume fraction are reasonably consistent, despite significant swelling of the PMMA by tetralin. The only substantial anomaly is the large positive deviation of the osmotic pressure in the crystalline solid relative to that from simulations for the fcc hard sphere crystal. Because of our equation of state measurements, we believe that the PMMA-PHSA data, rather than the earlier data, may represent the hard sphere curve for low shear viscosities.

ACKNOWLEDGMENTS

We would like to thank Glenn Riechart for helping us with the density gradient column, Nan Yao with the TEM data, and Phil Segrè for his informative discussions. This research was funded by a NASA grant (NAG3-1762) and Graduate Student Researchers Program Fellowship (NGT3-52301).

[1] T. Gisler, S. F. Schulz, M. Borkovec, H. Sticher, P. Schurtenberger, B. D'Aguanno, and R. Klein, J. Chem. Phys. **101**, 9924 (1994).
[2] R. H. Ottewill, Langmuir **5**, 4 (1989).
[3] P. N. Pusey and W. van Megen, in *An Exxon Monograph: Physics of Complex and Supermolecular Fluids*, edited by S. A. Safrar and N. A. Clark (Wiley-Interscience, New York, 1987), p. 673.
[4] W. B. Russel and P. R. Sperry, Prog. Organic Coatings **23**, 305 (1994).
[5] S. E. Paulin and B. J. Ackerson, Phys. Rev. Lett. **64**, 2663 (1990).
[6] J. Mewis, W. J. Frith, T. A. Strivens, and W. B. Russel, AIChE J. **35**, 415 (1989).
[7] R. J. R. Cairns, R. H. Ottewill, D. W. J. Osmond, and I. Wagstaff, J. Colloid. Interf. Sci. **54**, 45 (1992).
[8] L. V. Woodcock, Ann. N.Y. Acad. Sci. **371**, 274 (1981).
[9] W. G. Hoover and F. H. Ree, J. Chem. Phys. **49**, 3609 (1968).
[10] K. E. J. Barrett, *Dispersion Polymerization in Organic Media* (Wiley, New York, 1975).
[11] P. N. Segrè, S. P. Meeker, P. N. Pusey, and W. C. K. Poon, Phys. Rev. Lett. **75**, 958 (1995).
[12] I. M. de Schepper, E. G. D. C. Cohen, and R. Verberg, Phys. Rev. Lett. **77**, 584 (1996).
[13] I. Moriguchi, K. Kawasaki, and T. Kawakatsu, J. Phys. (France) II **3**, 1179 (1983).
[14] E. Dickinson and R. Parker, J. Phys. (Paris) Lett. **49**, L229 (1985).
[15] R. McRae and A. D. J. Haymet, J. Chem. Phys. **88**, 1114 (1988).
[16] J. L. Barrat and J. P. Hansen, J. Phys. (Paris) **47**, 1547 (1986).
[17] P. G. Bolhuis and D. A. Kofke, Phys. Rev. E **54**, 634 (1996).
[18] P. N. Pusey, J. Phys. (Paris) **48**, 709 (1987).
[19] S. M. Underwood, J. R. Taylor, and W. van Megen, Langmuir **10**, 3550 (1994).
[20] P. N. Pusey, in *Liquids, Freezing, and the Glass Transition*, edited by J. P. Hansen, D. Levesque, and J. Zinn-Justin (Elsevier, Amsterdam, 1991).
[21] W. B. Russel, J.-X. Zhu, and V. Manoharan (unpublished).
[22] L. Antl, J. W. Goodwin, R. D. Hill, R. H. Ottewill, S. M. Owens, and S. Papworth, Colloids Surf. **17**, 67 (1986).
[23] N. F. Carnahan and K. E. Starling, J. Chem. Phys. **51**, 635 (1969).
[24] K. R. Hall, J. Chem. Phys. **57**, 2252 (1972).
[25] R. Piazza, T. Bellini, and V. Degiorgio, Phys. Rev. Lett. **71**, 4267 (1993).
[26] M. A. Rutgers, J. H. Dunsmuir, J.-Z. Xue, W. B. Russel, and P. M. Chiakin, Phys. Rev. B **53**, 5043 (1996).
[27] J. C. Russ, *The Image Processing Handbook* (CRC Press, Boca Raton, FL, 1992), p. 210.
[28] W. B. Russel, D. A. Saville, and W. R. Showalter, *Colloidal*

Dispersions (Cambridge University Press, Cambridge, 1989).
[29] J. F. Brady, J. Chem. Phys. **99**, 567 (1993).
[30] G. K. Batchelor, J. Fluid Mech. **83**, 97 (1977).
[31] C. G. de Kruif, E. M. F. van Iersel, A. Vrij, and W. B. Russel, J. Chem. Phys. **83**, 4717 (1985).
[32] S. Mitaku, T. Ohtsuki, K. Hirakawa, H. Handa, and K. Okano, J. Faculty of Engineering, The University of Tokyo (B) **XXXIV**, 605 (1978).
[33] B. H. Zimm and D. M. Crothers, Proc. Natl. Acad. Sci. U.S.A. **48**, 905 (1962).
[34] L. Gary Leal, *Laminar Flow and Convective Transport Processes: Scaling Principles and Asymptotic Analysis* (Butterworth-Heinemann, Boston, 1992).
[35] Y. S. Papir and I. M. Krieger, J. Colloid. Interf. Sci. **34**, 126 (1970).
[36] M. E. Woods and I. M. Krieger, J. Colloid. Interf. Sci. **34**, 91 (1970).
[37] J. C. van der Weff and C. G. de Kruif, J. Rheol. **33**, 421 (1989).
[38] T. Shikata and D. S. Pearson, J. Rheol. **38**, 601 (1994).